Polymer Testing 153 (2025) 109040

Contents lists available at ScienceDirect

Polymer Testing

journal homepage: www.elsevier.com/locate/polytest

Tailored performance optimization of *p*-aramid copolymer fibers: From strength to thermo-chemical durability

Min Woo Kim [a,1], Hyeonjeong Kim [b,1], Jaegeun Lyu [a], Howon Choi [c], Juyoung Kim [a], Donghoon Lee [a], Dae Young Lim [d], Ji Ho Youk [c,*], Youngho Eom [b,**], Han Gi Chae [a,***]

[a] Department of Materials Science and Engineering, Ulsan National Institute of Science and Technology (UNIST), Ulsan, 44919, Republic of Korea
[b] Department of Organic and Nano Engineering, Human-Tech Convergence Program, Hanyang University, Seoul, 04763, Republic of Korea
[c] Department of Chemistry and Chemical Engineering, Education and Research Center for Smart Energy and Materials, Inha University, Incheon, 22212, Republic of Korea
[d] Department of Human and Culture Convergence Group, Korea Institute of Industrial Technology (KITECH), Ansan, 15589, Republic of Korea

ARTICLE INFO

Keywords:
p-Aramid copolymer
Positional isomer (3,4′-ODA, 4,4′-ODA)
Molecular design
Co-p-aramid fiber
Tailoring property

ABSTRACT

Para: aramid (*p*-aramid) fibers, traditionally used in bulletproof vests because of their exceptional strength and modulus, are now widely utilized in optical cables and the aerospace industry. This growing demand driven by advanced applications requires precise performance grading to meet diverse operational requirements. This study proposes a rational copolymerization strategy for tailoring the properties of *p*-aramid copolymer (*co-p*-aramid) fibers by adjusting the ratio of 3,4′-oxydianiline (3,4′-ODA) and 4,4′-oxydianiline (4,4′-ODA). While 3,4′-ODA enhances mechanical strength, 4,4′-ODA improves thermo-chemical stability. For high-strength applications, *co-p*-aramid fibers synthesized with 3,4′-ODA as the sole comonomer achieve a tensile modulus and tensile strength of 80.4 and 3.1 GPa, respectively. For superior thermo-chemical resistance, fibers with a 3,4′-ODA:4,4′-ODA molar ratio of 2:8 exhibit the highest stability, with a decomposition temperature of 484.1 °C, which is 25.7 °C higher than that of the sole 3,4′-ODA-based fiber. Further, these fibers demonstrate strong chemical durability, retaining 42 % and 98 % of their tensile strength and modulus, respectively, after 24 h in 60 wt% nitric acid, whereas the latter retains only 15 % and 61 %. These findings confirm that molecular design using positional isomers effectively fine-tunes the performance of *co-p*-aramid fibers, establishing a foundation for developing customized high-performance fibers.

1. Introduction

The development of high-strength and/or high-modulus fibers is considered a top priority in the fiber industry for several decades since fiber-reinforced plastics have been recognized as key materials in high-tech applications such as aviation, aerospace, military, and electric vehicles [1–6]. Representative examples include carbon fibers, ultra-high-molecular-weight polyethylene, and aramid fibers, each distinguished by their exceptional tensile strength and stiffness [1–8]. However, emerging advanced industries require fibers with specialized functionalities beyond their mechanical performance, including heat resistance, electrical insulation, and chemical durability [9–12]. Accordingly, future developments in the fiber industry must move beyond mechanical performance enhancement alone to precisely controlling tailored properties aligned with specific industrial needs.

Aramid fibers such as poly(*p*-phenylene terephthalamide) (PPTA) are composed of polymers with abundant aromatic rings and strong intermolecular hydrogen bonds [13,14]. This unique molecular architecture inherently imparts excellent thermal and chemical resistance along with superior mechanical properties, which makes aramid fibers highly suitable for a wide range of high-performance applications. Further, this distinctive molecular structure of aramid fibers imparts unique characteristics. Representative examples include *para*-aramid (*p*-aramid), *meta*-aramid (*m*-aramid), and copolymerized *p*-aramid (*co-p*-aramid)

* Corresponding author.
** Corresponding author.
*** Corresponding author.
E-mail addresses: youk@inha.ac.kr (J.H. Youk), eomyh@hanyang.ac.kr (Y. Eom), hgchae@unist.ac.kr (H.G. Chae).
[1] These authors equally contributed to the work.

https://doi.org/10.1016/j.polymertesting.2025.109040
Received 20 August 2025; Received in revised form 28 October 2025; Accepted 11 November 2025
Available online 12 November 2025

fibers [13–19]. While *p*-aramid fibers are widely recognized for their exceptional mechanical strength, *m*-aramid fibers are noted for their superior flame resistance and electrical insulating properties [13–19]. These specific performance attributes enable *p*-aramid and *m*-aramid fibers to be predominantly utilized in the manufacture of bulletproof vests and firefighting apparel, respectively. Meanwhile, *co-p*-aramid fibers (CAFs) are synthesized using 3,4′-oxydianiline (3,4′-ODA) as a third comonomer, providing a kink structure to the *p*-aramid backbone [17–19]. Interestingly, this molecular design improves several attributes such as chemical stability, flexibility, and fatigue resistance, while preserving comparable mechanical strength and modulus. In addition, introducing the kink structure significantly improves solubility, which enables *co-p*-aramid to dissolve in *N*-methyl-2-pyrrolidone (NMP) instead of using strong sulfuric acid. Hence, CAFs have gained significant research attention as promising substitutes for conventional *p*-aramid fibers.

Recent studies have further broadened the design space of *co-p*-aramids by incorporating a wide range of novel comonomers beyond 3,4′-ODA (Table S1). For instance, benzocyclobutane derivatives undergo thermal cross-linking [20], which enhances compressive strength and creep resistance, whereas benzobisoxazole moieties improve intermolecular interactions and molecular orientation, thereby simultaneously increasing tensile strength and thermal stability [21]. Likewise, benzimidazole-based units create extensive hydrogen bonding networks that reinforce chain cohesion and significantly improve tensile properties [22–24]. In addition, several studies have explored hybridization strategies using ODA-derived comonomers. Copolymerization of 3,4′-ODA with benzimidazole has yielded fibers that exhibit improved chain orientation and tensile properties [25], while 4,4′-oxydianiline (4,4′-ODA) has primarily been employed to improve processability by incorporating ether linkages into the polymer backbone [26].

In this study, unlike the aforementioned approaches, we propose a simple yet effective strategy that adjusts the relative ratio of the two positional isomers of ODA; 3,4′-ODA and 4,4′-ODA. This copolymerization approach allows precise control over fiber performance through the systematic control of monomer composition, thereby enabling tailored enhancements in mechanical, thermal, and chemical properties [27] (Fig. 1). In contrast to conventional performance grading methods or post-treatment strategies, our molecular-level approach enables the direct modulation of fiber characteristics during synthesis. An increased proportion of 3,4′-ODA improved mechanical strength, whereas higher 4,4′-ODA content enhances thermal and chemical resistance. This tunable copolymerization strategy provides a scalable and versatile approach to develop next-generation aramid fibers with application-specific performance profiles.

2. Experimental

2.1. Materials

p-Phenylenediamine (PPD, >99 % Amino-Chem), 3,4′-ODA (>99.5 %, Wakayama Seika Kogyo), 4,4′-ODA (>99.5 %, Wakayama Seika Kogyo), terephthaloyl chloride (TPC, >99 %, Sigma-Aldrich), anhydrous NMP (>99.5 %, Sigma-Aldrich), and calcium hydroxide ($Ca(OH)_2$, >95 %, Sigma-Aldrich) were used as received.

2.2. Synthesis of co-p-aramid solutions

A series of *co-p*-aramid solutions (CAs) were synthesized through a direct polycondensation reaction, employing TPC as a diacid and a mixture of PPD, 3,4′-ODA, and 4,4′-ODA as diamines. The CAs were designated as CA-M*x*P*y*, where *x* and *y* represent molar ratios of 3,4′- and 4,4′-ODAs, respectively. (3,4′-ODA/4,4′-ODA = 100/0, 80/20, 60/40, 40/60, and 20/80 (mol/mol)) The synthesis was conducted in a 2 L, dual-jacketed, four-neck flask reactor within a nitrogen-filled glove box. This reactor was equipped with a nitrogen inlet and a mechanical stirrer. To illustrate a typical polymerization process, CA-M6P4 [3,4′-ODA/4,4′-ODA (60/40 mol/mol)] was synthesized under the following conditions: Initially, the reactor was charged with 6.397 g of PPD (59.157 mmol), 7.107 g of 3,4′-ODA (35.494 mmol), 4.738 g of 4,4′-ODA (23.663 mmol),

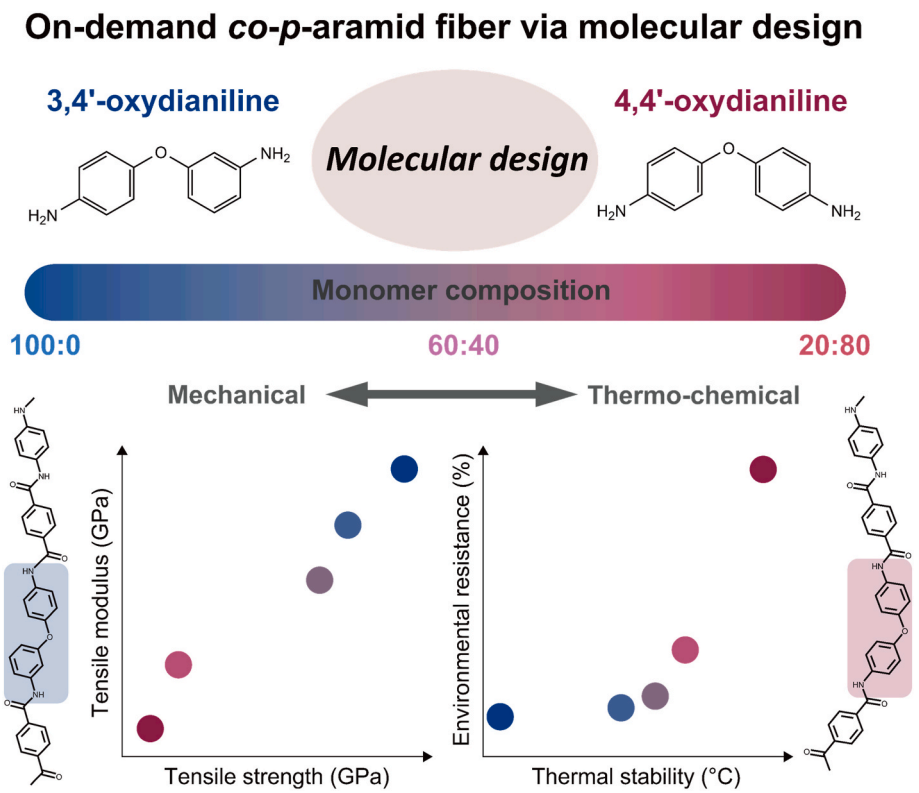

Fig. 1. Molecular design for CAFs that enables tunable properties for on-demand high-performance applications.

and 450 mL of NMP. Subsequently, the mixture was stirred vigorously at 25 °C under a continuous flow of dry nitrogen to ensure the complete dissolution of all reactants. 24.020 g of the powdered TPC (118.313 mmol) was rapidly added to the reactor. The reaction progress was monitored by measuring the torque of the mixture at a stirring speed of 300 rpm. When the desired torque level was reached, the stirring speed was reduced to 10 rpm and a dispersion of 8.766 g of $Ca(OH)_2$ in 45 ml of NMP was added quickly. Following this addition, the temperature of the mixture increased to 80 °C. The mixture was stirred for an additional 2 h to ensure the complete neutralization of a hydrochloric acid byproduct; this resulted in a polymer solution with a concentration of 6.0 wt%.

2.3. Spinning and heat drawing process

Dry-jet wet spinning was conducted using a custom-built spinning setup equipped with a syringe pump (0.3 mL/rev) and a spinneret of 12 holes (200 μm diameter). The polymer solution was extruded at a controlled flow rate of 0.8 mL/min, which corresponded to 2 m/min per hole. The air gap was fixed at 10 mm, and the spinning temperature was maintained in the range of 70–80 °C. The extruded filaments were first coagulated in a 10 °C deionized (DI) water bath, then sequentially passed three washing baths filled with 20 °C DI water and finally collected by the winder. The as-spun draw ratio (SDR) was adjusted stepwise: 1.10 in the coagulation bath, increased to 1.20 and 1.35 in the first and second washing baths, and finally set to 1.50 in the third washing bath and at the winder. The obtained filaments were further washed in DI water for 24 h to remove residual NMP and subsequently treated with a finish oil for antistatic and condensing purposes. And then, the CAFs with the most stable and highest post drawing ratio (PDR) were fabricated through a post drawing process using a tubular electric furnace at 460 °C. CAFs were also named as CAF-MxPy according to the molar ratio of ODA, and CAF-M10P0, M8P2, M6P4, M4P6, and M2P8 were obtained with Total drawing ratio (TDR) 9, 9, 9, 3, and 2, respectively. (TDR = SDR × PDR)

2.4. Environmental test

Environmental resistance tests were conducted using acids, bases, and steam. The prepared CAFs were immersed in a 60 wt% nitric acid solution for 24 h and in a 50 wt% sodium hydroxide aqueous solution for 120 h. In addition, DI water was evaporated using a 160 °C hot plate, and a steam test was conducted for 120 h in a saturated environment.

2.5. Characterization

The molecular characterization of the synthesized CAs was conducted using gel permeation chromatography (Young Lin Chrozen HPLC system). This analysis determined the number-average molecular weights (M_n) and polydispersity indice (PDI) of CA. A 0.01 M LiBr/NMP solution was used as the mobile phase, and it was maintained at 80 °C with a flow rate of 1.0 mL/min. Poly(methyl methacrylate) standards were used for column calibration. Fourier-transform infrared spectroscopy (FTIR, Cary 670, Agilent Technologies) was performed in accumulated attenuated total reflectance mode, accumulating 256 scans for each infrared (IR) spectrum. The rheological properties of the CAs were measured using a rheometer (Haake MARS III, Thermo Scientific) from 20 to 80 °C using a cub and bob geometry with a CC16 DIN Ti. Mineral oil was used for preventing solvent evaporation. A frequency sweep was conducted over a range of 0.05–500 rad/s. The gap and strain level were 3.318 mm and 5 %, respectively. Field-emission scanning electron microscopy (SEM, SU7000, Hitachi Ltd.) was used for analyzing the surface and cross-section of the CAFs at an accelerating voltage of 10 kV after sputter coating with platinum. The mechanical properties were measured using FAVIMAT+ (Textechno). For measurement conditions, the pretension was set to 0.5 cN, gauge length was set to 20 mm, and strain rate was set to 20 mm/min. The tensile strength was determined by measuring the force required to break the fibers. In addition, the tensile modulus was measured by calculating the slope of the stress–-strain curve in the elastic region of 0.3 %–0.6 % elongation. The linear density was measured using resonance frequency with a vibroscope under the same conditions as those for the tensile property measurements. Thermogravimetric analysis (TGA, Q500, TA Instruments) was used for determining the degradation temperature of the fibers. The amount of sample was ~10 mg, measured using a platinum pan and cup, at a ramping rate of 5 °C/min from 50 to 900 °C. In addition, isothermal TGA was performed for evaluating thermal stability, and the residual weight was determined by isothermal treatment for 30 min after a ramping rate of 10 °C/min was achieved up to 500 °C. In addition, Dynamic mechanical analysis (DMA, Q800, TA Instruments) was used to determine the glass transition temperature (T_g). The gauge length was set to 20 mm, and the ramping rate was measured at 5 °C/min from 50 to 400 °C at a 0.1 % strain rate. The activation energy (E_a) was measured at 1, 5, and 10 Hz and calculated using the Arrhenius law. The creep test was performed at 40 % of its tensile strength for 100 min. The wide-angle X-ray diffraction (WAXD) and small-angle X-ray scattering (SAXS) measurements were obtained using the PLS-II 6D UNIST-PAL beamline at the Pohang Accelerator Laboratory (PAL) in Korea. The crystallinity, Herman's orientation factor, crystallite size, and d-spacing of the crystal plane were obtained, and the X-ray energy was 18.986 keV. The misorientation angles of the fibrils were determined using SAXS analysis with an X-ray energy of 11.564 keV. The WAXD and SAXS sample-to-detector distances were ~240 and 3070 mm, respectively. The crystallinity was calculated by utilizing crystal, mesophase, and amorphous peak obtained by deconvolution of the WAXD 1D profile. The orientation factor of (006) plane (f_{006}) was calculated using Herman's orientation factor through an azimuthal scan for the (006) plane, where ϕ is the azimuthal angle at $2\theta \approx 42°$ (Eqs. S1 and S2). D-spacings of the (110) and (006) plane (d_{110}, d_{006}) were obtained from Bragg's law where λ and θ represent the wavelength and Bragg's angle, respectively (Eq. S(3)). The crystallite size (L_{110}, L_{006}) was calculated by Scherrer's equation, where β represents the full width at half maximum, and K represents the Scherrer constant, which is assumed to be 0.9 (Eq. S(4)). The misalignment angles of the fibrils were determined using the Ruland streak method. The fibrils were presumed to have cylindrical structures. When aligned along the axial direction, the fibrils were scattered in the equatorial direction. An imperfect alignment of fibrils along the axial direction resulted in a fan-shaped streak in the equatorial direction. The misalignment angle of the fibril can be determined by analyzing an azimuthal scan of an equatorial streak, and the azimuthal distribution can be described as a function of s in the reciprocal space and be characterized based on the observed integral breadth (B_{obs}) (Eq. S(5)). $I(s,\varphi)$ in the azimuthal scan is obtained at scattering vector $s = (2\sin\theta)/\lambda$, where 2 θ and λ represent the scattering angle and wavelength, respectively. Here, φ is defined as the azimuthal angle, $I(s,\varphi)$ is fitted using Gaussian–Lorentz distribution, and φ_{max} represents the angle at which the peak maximum is found. The misorientation angle (B_g) is defined as the square root of the slope obtained from linear fitting (Eq. S(6)).

3. Results and discussion

3.1. Molecular engineering of CAs using positional isomeric ODAs

Conventional *p*-aramid fibers are composed of PPTA synthesized via a polycondensation reaction between PPD and TPC [13]. In this study, ODA was introduced as a comonomer to modulate the symmetry, backbone rigidity, and intermolecular interactions of the polymer chains (Fig. 2a) [19]. We propose a molecular engineering strategy that controls the ratio of ODA positional isomers for precisely tailoring the final performance of CAFs. 3,4′-ODA and 4,4′-ODA share the same molecular formula; however, they differ in the positioning of their amine groups. In

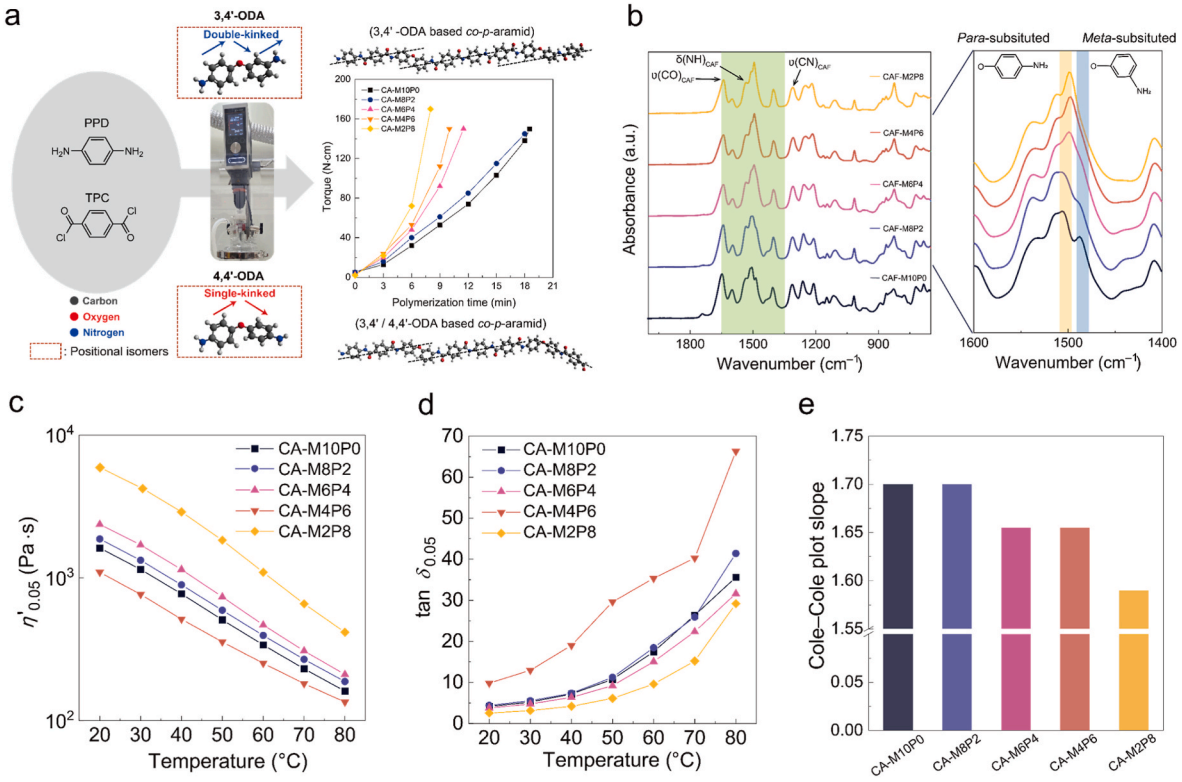

Fig. 2. Structural and rheological properties of CAs with varying 3,4′-ODA:4,4′-ODA ratios. (a) Schematic illustration of polymerization process for CAs incorporating ODA positional isomers. (b) FTIR spectra of CAFs, which highlights aromatic peaks corresponding to *para*- (yellow) and *meta*- (blue) substituted structures. (c) Dynamic viscosity (η') and (d) tan δ profiles of CAs. (e) Comparison of Cole–Cole slopes of CAs.

3,4′-ODA, amines occupy *meta-para* positions, which leads to a "double-kinked" molecular geometry, whereas in 4,4′-ODA, the *para-para* arrangement leads to a "single-kinked" structure [28]. CAs were synthesized using three amine monomers, namely, PPD, 3,4′-ODA, and 4,4′-ODA. The PPD accounted for 50 mol% of the total amine content, and the remaining 50 mol% was composed of 3,4′-ODA and 4,4′-ODA. The CAs are designated as CA-M*x*P*y*, where *x* and *y* represent molar ratios of 3,4′- and 4,4′-ODAs, respectively. CAFs are referred to as CAF-M*x*P*y* in the subsequent discussion. A total of five CAs were synthesized with varying 3,4′-ODA:4,4′-ODA molar ratios ranging from 10:0 to 2:8. Their molecular characteristics, including M_n and PDIs, are summarized in Table S2. The M_n values ranged from 299,100 to 324,700 g/mol, while the corresponding PDIs were between 2.03 and 2.14. Slight variations in molecular weight are attributed to the different reactivities of the ODA positional isomers during polymerization.

Chemical structures of the CAFs were investigated using FTIR spectroscopy, with a specific emphasis on varying molar ratios of 3,4′-ODA to 4,4′-ODA (Fig. 2b). While all CAFs exhibited comparable chemical compositions, their chain configurations differed significantly because of structural variations introduced by positional isomers. Characteristic absorption bands were observed at 1646 cm^{-1} (C=O stretching), 1537 cm^{-1} (N–H bending), and 1310 cm^{-1} (C–N stretching), which confirmed the formation of aramid linkages [29]. Differences in chain configurations were reflected in the vibrational modes of benzene rings. In CAFs containing a higher fraction of 4,4′-ODA, the symmetrical *para-para* arrangement of the benzene rings gave rise to a single peak at 1500 cm^{-1}. In contrast, the asymmetry in the asymmetric *meta-para* arrangement in 3,4′-ODA induced splitting of this vibrational mode, which resulted in two distinct peaks at 1500 and 1486 cm^{-1} [30]. Consequently, CAs with higher 3,4′-ODA content (CAF-M10P0, -M8P2, and -M6P4) displayed apparent band splitting, whereas those enriched in 4,4′-ODA (CAF-M4P6 and -M2P8) showed negligible splitting, which is indicative of greater structural regularity.

The rheological behavior of CAs was analyzed as a function of comonomer composition (Fig. 2c–e and S1–S3). In contrast to conventional *p*-aramid/H_2SO_4 solution systems that typically form anisotropic liquid crystalline phases, *co-p*-aramids are organosoluble in NMP, yielding isotropic (nonliquid crystalline) solutions [13,19]. These isotropic solutions exhibited upper critical solution temperature behaviors, characterized by a decrease in viscosity and an increase in the loss tangent (tan δ, which is the ratio of viscous to elastic response) with increasing temperature (Fig. 2c and d, S1, and S2). With increasing 4,4′-ODA content, the viscosity generally increased and tan δ decreased because enhanced chain rigidity restricts molecular mobility and strengthens the elastic response; however, a slight non-monotonic deviation observed for the M4P6 composition is likely due to its relatively lower molecular weight. Cole–Cole plots were constructed for each formulation to evaluate solution homogeneity (Fig. 2e and S3). In this analysis, the slope between the storage modulus (G′) and loss modulus (G'') on a logarithmic scale serves as an indicator of solution uniformity, approaching 2 for ideally homogeneous systems [31]. Within the same comonomer system, it is directly correlated with the microstructural development and mechanical performance of the resulting fibers [32]. In this study, the Cole–Cole analysis was used primarily as supporting evidence to qualitatively assess solution uniformity with varying comonomer composition. The slope of Cole–Cole plots decreases from 1.70 to 1.59 when the fraction of 4,4′-ODA increases from M10P0 to M2P8, which indicates a reduction in solution homogeneity. This trend can be attributed to the molecular characteristics of ODA monomers: the more rigid chain structure of CAs with higher 4,4′-ODA fractions leading to reduced solubility in NMP, thereby diminishing solution homogeneity [30,33]. The incorporation of ODA units enables the fine tuning of key properties such as solubility, thermal stability, and chemical resistance while maintaining the intrinsic mechanical strength of *p*-aramid fibers.

3.2. Effect of molecular engineering on the microstructure of CAFs

CAFs with varying comonomer ratios were fabricated successfully using dry-jet wet spinning, followed by thermal post-heat drawing (Fig. 3a and S4). Structural disparity between the two ODA comonomers resulted in differential drawability during fiber formation. Specifically, CAF-M10P0, CAF-M8P2, and CAF-M6P4 achieved a Total drawing ratio (TDR) of 9, indicating excellent stretchability. In contrast, CAF-M4P6 and CAF-M2P8 exhibited reduced drawability with TDR values of 3 and 2, respectively. One-dimensional WAXD profiles and corresponding two-dimensional patterns of CAFs are presented in Fig. 3b and S5–S7. CAFs exhibit diffraction peaks at $2\theta \approx 20$, 22, 14, 27, and 42° in X-ray patterns, which corresponds to (110) and (200) planes in the equatorial direction, and the (002), (004), and (006) planes in the meridional direction, respectively [34,35]. Distinct meridional diffractions indicate a higher degree of molecular orientation in the longitudinal direction [19,36]. Among the three meridional peaks, the (006) diffraction peak was selected for calculating the orientation factor and crystallite size. Based on deconvoluted spectra from 1D equatorial patterns (Fig. S7), the relative intensity ratios of (006)/(110) diffractions were plotted as functions of the comonomer composition (Fig. 3c). CAF-M10P0 exhibits a ratio of 1.31, which gradually decreases to 0.36 with an increase in the fraction of 4,4′-ODA. This trend indicates that relatively flexible *co-p*-aramid chains, enriched with 3,4′-ODA units, facilitate the formation of extended chain conformations along the fiber axis.

For a quantitative assessment, crystallite sizes and orientation factors were determined using (006) diffraction (Fig. 3e and Table S3), with orientation factors obtained from azimuthal scans (Fig. 3d). Both

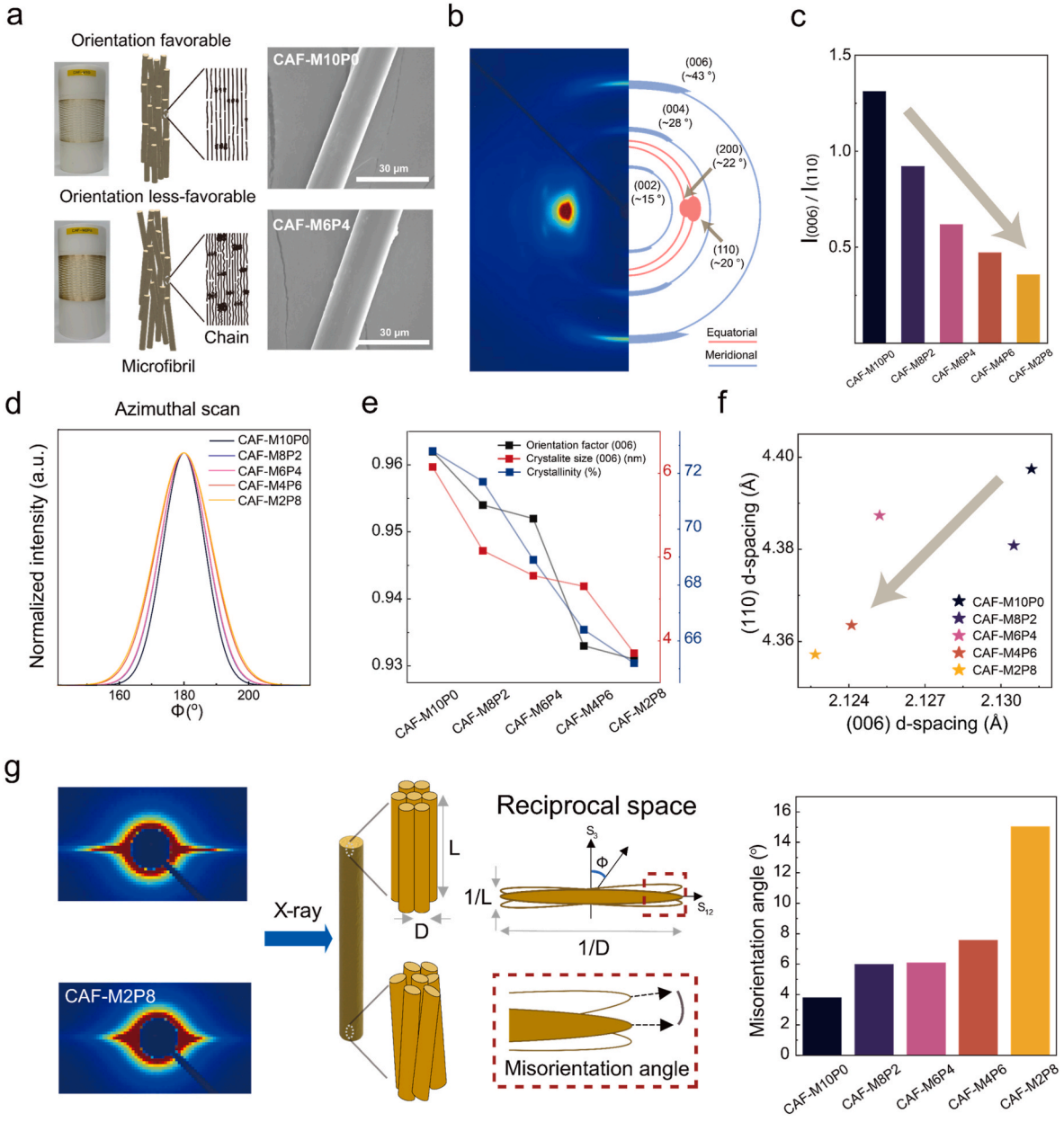

Fig. 3. Microstructural analysis of CAFs. (a) Surface image and schematic illustration for microstructures of CAFs. (b) 2D WAXD pattern of CAF-M6P4 indicating characteristic diffractions including (110), (200), (002), (004), and (006) crystal planes. (c) Intensity ratio between (006) and (110) planes obtained from the peak deconvolution of integrated 1D scan profiles. (d) Azimuthal scan profiles of the (006) plane. (e) Comparison of microstructural parameters including orientation factor ((006) plane), crystallite size ((006) plane), and overall crystallinity. (f) D-spacings for (110) and (006) planes of CAFs. (g) Fibril misorientation angles calculated from SAXS analysis using the Ruland method.

parameters increased notably with a higher 3,4′-ODA content, ranging 3.9–6.1 nm for a crystallite size, and 0.931–0.962 for the orientation factor. While TDRs substantially affect microstructural evolution, fiber stretchability is fundamentally governed by molecular flexibility. From a molecular perspective, a higher concentration of kinked structures hinders chain extension because of the reduced rigidity [16]; however, in the case of CAFs, the double-kinked 3,4′-ODA moiety promotes chain extension when subjected to sufficient stretching, as indicated in Fig. 3a. This can be attributed to its inherent flexibility and large conformational freedom, which facilitate axial alignment during heat drawing, while the double-kinked configuration enables the chains to adopt a more linear conformation, thereby further promoting chain extension [25,28,37]. In addition, the abundant aromatic rings and amide groups along the polymer backbone enable strong secondary interactions such as π-π stacking and hydrogen bonding, which contributes to the longitudinal alignment of the extended chains [38,39]. Crystallinity exhibited a similar trend to the two structural parameters, increasing from 65.2 % (CAF-M2P8) to 72.8 % (CAF-M10P0). In contrast, the d-spacings of the (110) and (006) planes, representing interplanar distances in a crystal lattice, exhibited the opposite trend (Fig. 3f). Among the five CAFs, CAF-M2P8, which contains the highest fraction of 4,4′-ODA, shows the smallest d-spacings for the (110) and (006) planes (4.35 and 2.21 Å, respectively). These contrasting trends indicate that the 3,4′-ODA component plays a dominant role in facilitating microstructural development during fiber drawing while the rigid 4,4′-ODA moiety enhances molecular packing within the crystal lattice [40,41].

In addition to the crystallographic analysis, the alignment of microfibrils was examined by SAXS analysis (Fig. 3g and Table S4). All CAFs exhibited pronounced equatorial streaks, which is indicative of microfibrils aligned parallel to the fiber axis (Fig. S8) [24,34,42]. The sharpness and elongation of these streaks correlate with the degree of microfibril orientation. According to the Ruland method (Fig. 3g), CAF-M10P0, which exhibited the sharpest streak, showed the lowest misorientation angle of 3.8°, whereas the broader streak observed in CAF-M2P8 corresponded to a higher angle of 15.1°. These results confirm that the comonomer composition and resulting chain conformations significantly affect the alignment of both crystallites and microfibrils across different structural length scales.

3.3. Microstructural insights into the mechanical properties of CAFs

The effect of comonomer composition on the mechanical properties of CAFs was investigated by establishing correlations between their microstructural features and macroscopic properties. The stress–strain

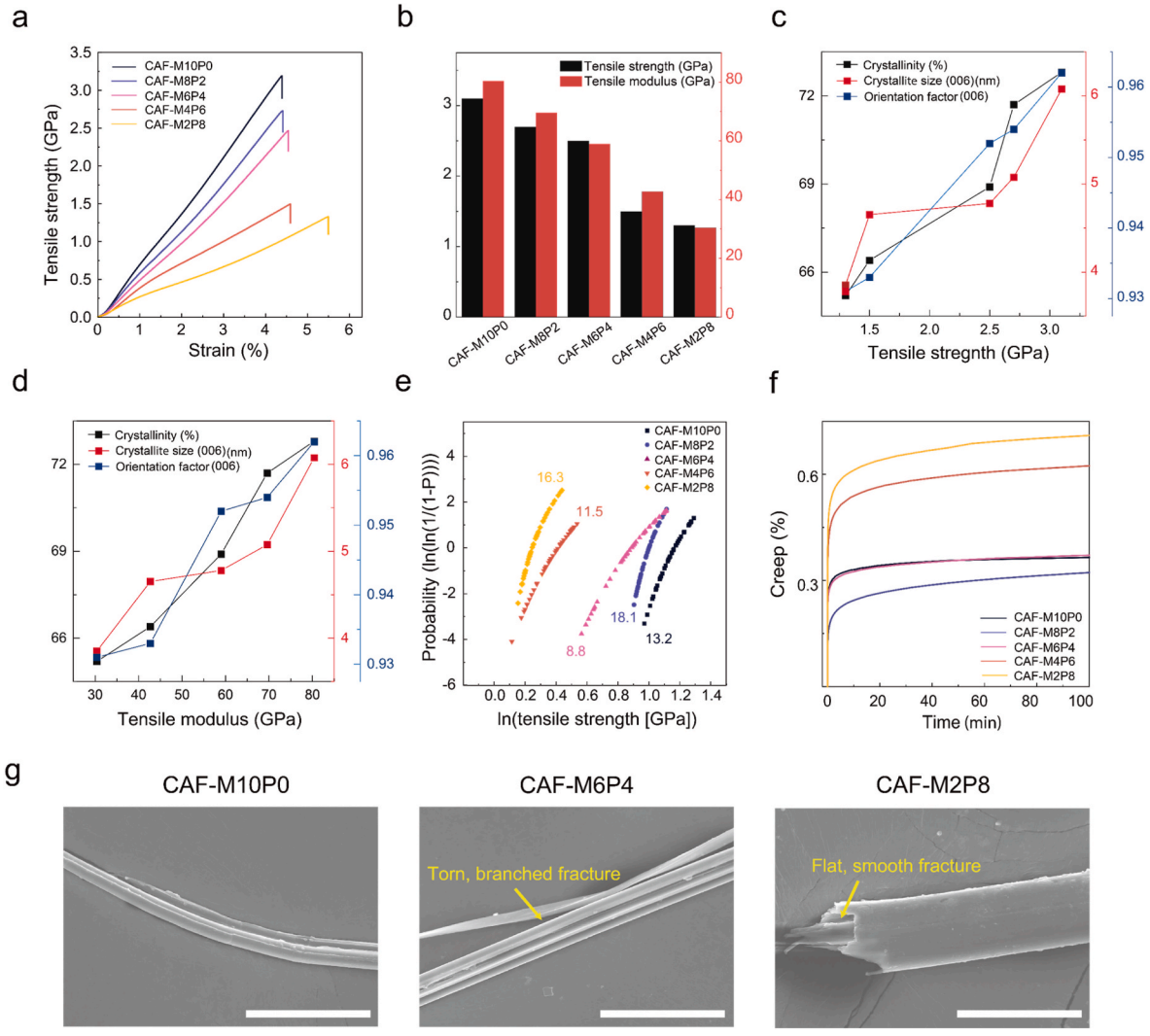

Fig. 4. Mechanical performance and structure–property relationships of CAFs. (a) Representative stress–strain curves. (b) Tensile strength and tensile modulus of CAFs. (c) and (d) Correlation between tensile strength and modulus with microstructural parameters including crystallinity, crystallite size ((006) plane), and orientation factor ((006) plane). (e) Weibull modulus of CAFs. (f) Creep strain behavior under sustained loading. (g) SEM images of fracture surfaces of CAFs. (scale bar = 50 μm).

curves shown in Fig. 4a indicate that increasing the fraction of 3,4′-ODA leads to notable enhancements in both the tensile modulus (*E*) and tensile strength (TS). Quantitative variations in *E* and TS across different sample series are presented in Fig. 4b and Table S5, and their correlations with three key microstructural parameters, i.e., crystallinity, crystallite size, and orientation factors, are systematically analyzed in Fig. 4c and d. A near-linear increase in both *E* and TS with rising 3,4′-ODA content is observed. Comparing CAF-M2P8 (lowest 3,4′-ODA content) and CAF-M10P0 (highest 3,4′-ODA content), *E* and TS increased by 2.5-fold (from 30 to 80 GPa) and 2.8-fold (from 1.2 to 3.1 GPa), respectively.

In bulk polymers, improved mechanical properties are attributed to incorporating rigid chain segments [43,44], and the mechanical performance of fibers is often affected by the extent of microstructural development such as molecular orientation and crystalline morphology [15,34,45]. Interestingly, the strong correlation between mechanical properties and three aforementioned microstructural parameters in CAFs suggests that fine tuning of mechanical performance can be effectively achieved through microstructural control (Fig. 4c and d). Among these, *E* exhibits a stronger dependence on overall crystallinity, whereas TS shows a more pronounced correlation with the orientation factor. This tendency aligns with the underlying mechanisms that govern the tensile behavior of fiber system. Unlike the well-established relationship between the modulus and crystallinity, the strength-orientation correlation is characteristic of fiber systems because failure mechanisms primarily govern tensile strength (being a high-strain property) [46]. In this context, chains in the tail of the orientation distribution act as stress concentrators that trigger strain localization and crack initiation, while higher orientation narrows this tail and thereby reduces structural defects. Consistently, previous studies have reported that improved chain orientation leads to enhanced tensile strength. [24,46,47]. In this regard, the observed strength-orientation relationship may be attributed to improved structural homogeneity. This uniformity in performance was supported by the Weibull modulus analysis (Fig. 4e). In addition, CAFs with higher 3,4′-ODA content demonstrated reduced creep deformation under creep testing conditions (40 % of the tensile strength for 100 min) (Fig. 4f), and this can be attributed to inhibited chain slippage resulting from increased fiber alignment. Fractographic analysis using SEM (Fig. 4g) revealed that well-aligned fibers exhibited rough and branched fracture surfaces, impeding the propagation of microcracks.

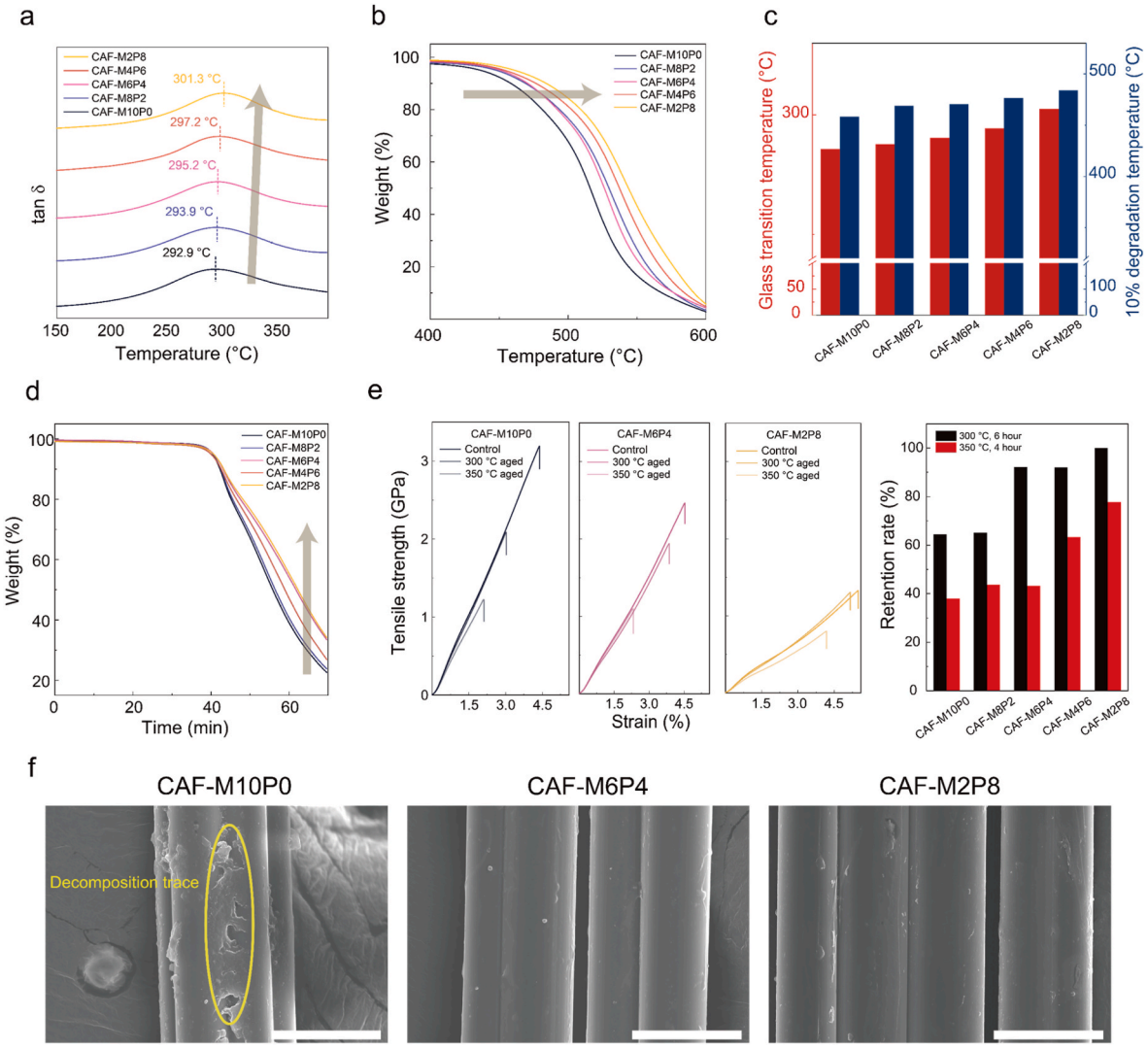

Fig. 5. Thermal stabilities and degradation behaviors of CAFs. (a) Tan δ curves for as-spun fibers. (b) TGA curves showing weight loss behavior. (c) Glass transition and 10 % degradation temperature. (d) Isothermal TGA curves for 30 min at 500 °C. (e) Stress–strain curves and tensile strength retention after thermal aging at 300 °C for 6 h, and 350 °C for 4 h. (f) SEM images of CAFs exposed to 300 °C for 6 h (scale bar = 50 μm).

3.4. Thermo-chemical stability as a function of molecular configuration

In addition to their superior mechanical properties, *p*-aramid-based fibers exhibit exceptional thermal and chemical resistance due to the synergistic combination of an aromatic ring-rich, rigid backbone and strong intermolecular interactions [17,19]. As a reference material, PPTA fibers exhibit glass transition temperature (T_g) near 300 °C [48]. Although incorporating comonomers lowers chain regularity, CAFs can still retain higher levels of T_gs above 292 °C (Fig. 5a). Although the mechanical performance is enhanced by the 3,4′-ODA moiety, the thermal properties of CAFs are improved by increasing 4,4′-ODA fractions, as evidenced by DMA and TGA. The T_g values of CAFs increased gradually from 292.9 °C for CAF-M10P0 to 301.3 °C for CAF-M2P8 (Fig. 5a). Similarly, the activation energy for the glass transition exhibits a consistent trend, which increases from 120 to 200 kJ/mol with an increase in the 4,4′-ODA fraction (Fig. S9). Further, the 10 % degradation temperature notably increased by 25.7 °C, from 458.4 to 484.1 °C (Fig. 5b and c, and Table S6). These results confirm that incorporating 4,4′-ODA results in a more rigid polymer backbone, restricting thermal chain mobility and enhancing interchain

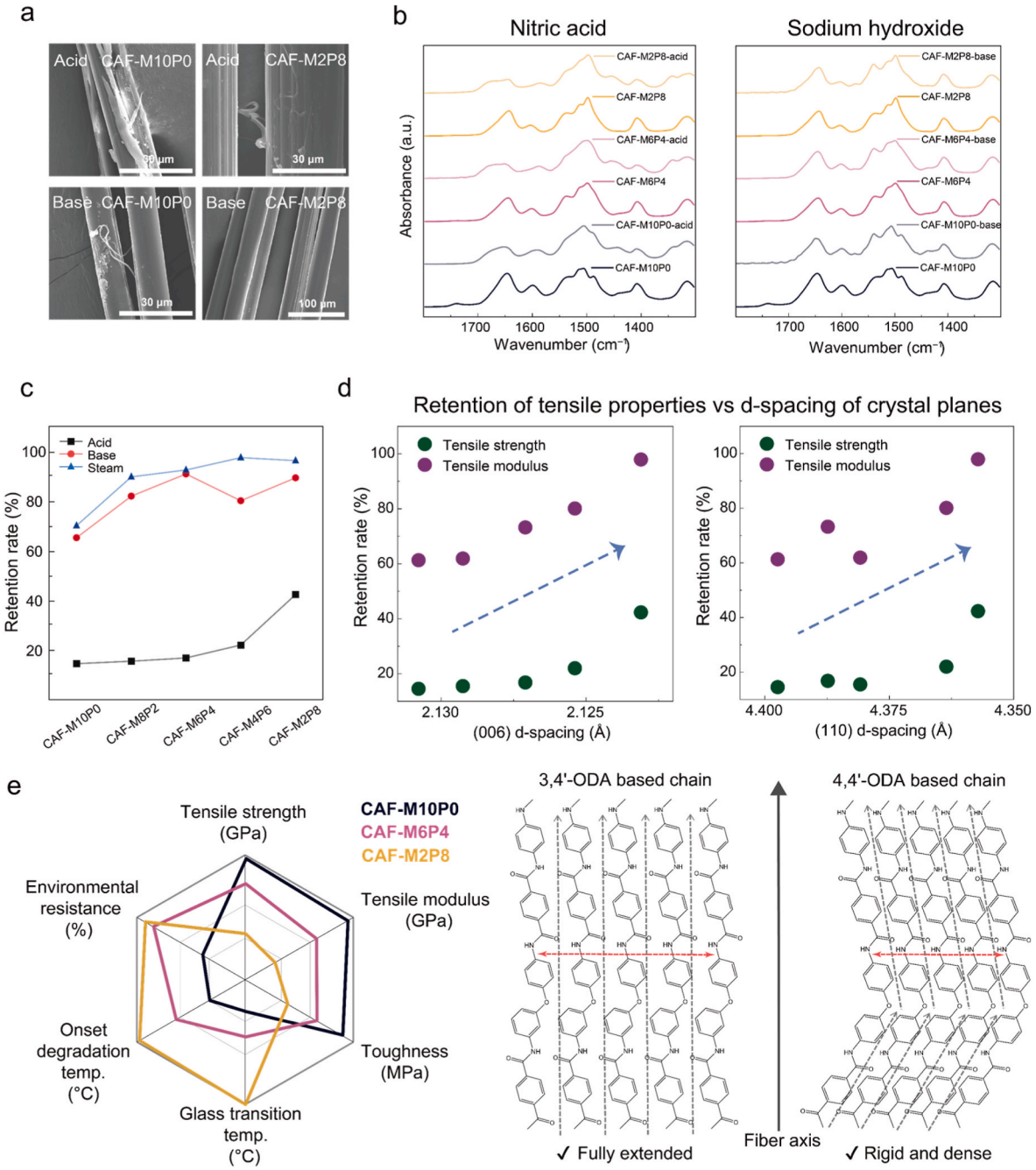

Fig. 6. Evaluation of the environmental resistance of CAFs. (a) SEM images of CAFs after acid (60 wt% nitric acid for 24 h) and base (50 wt% sodium hydroxide for 120 h) treatments. (b) FTIR spectra of CAFs collected pre- and post-treatment with an acid and a base. (c) Retention rate of tensile strength for acid, base, and steam treatments. (d) Correlation of tensile strength and tensile modulus retention rate in acid treated CAFs with d-spacing for the (006) and (110) crystal planes. (e) Radar chart comparing mechanical properties, thermal stability, and chemical resistance of CAFs, which illustrate performance tunability via monomer composition control. Schematic illustrations of 3,4′-ODA and 4,4′-ODA-based chains highlighting differences in backbone conformation and packing behavior, which supports their performances.

interactions, which suppresses thermal decomposition. This indicates that intrinsic structural properties of 4,4′-ODA determine its thermal stability.

The thermal durability of CAFs was investigated by evaluating the degradation of their mechanical properties during high-temperature exposure tests. The weight loss trend under an isothermal test at 500 °C for 30 min revealed a higher degree of retention for 4,4′-ODA-rich CAFs (Fig. 5d). After exposure at 300 °C for 6 h and 350 °C for 4 h, CAF-M10P0 underwent severe performance degradation, while the deterioration for CAF-M2P8 weakened, which is confirmed the retention rate of the TS values (Fig. 5e and Table S7). CAF-M10P0 exhibited a rapid decrease to approximately 64 % and 38 % at 300 °C and 350 °C, respectively, whereas CAF-M2P8, with a 4,4′-ODA-rich content, maintained 100 % and 77 % under the same conditions, indicating negligible degradation compared to the control. Furthermore, the SEM analysis results after thermal exposure (Fig. 5f) reveal that CAF-M10P0 exhibits pronounced surface decomposition. In contrast, the surface of CAF-M2P8 remains relatively clean, indicating its superior structural integrity. These findings confirm that the advantages of 4,4′-ODA observed in the thermal analysis translate into actual stability and reliability under realistic high-temperature conditions beyond conventional thermal indicators.

The chemical durability of the CAFs was assessed by immersing the fibers in harsh acidic or basic media (Fig. 6). The SEM images (Fig. 6a) revealed a significant surface degradation for CAF-M10P0 after a 24 h exposure to 60 wt% nitric acid and 120 h exposure to 50 wt% sodium hydroxide. However, CAF-M2P8 exhibited negligible surface etching under identical conditions, suggesting higher chemical resistance to both acidic and basic conditions. As characterized by FTIR analysis (Fig. 6b), CAFs with a lower fraction of 4,4′-ODA show diminishing amide bond peaks (C=O, N–H, and C–N), which can be attributed to hydrolysis [49]. Besides the morphological and structural changes, mechanical property retention tests were conducted under several harsh chemical conditions (Fig. 6c and S10, Tables S8 and S9). Following treatment with acid, base, and steam, fibers containing higher levels of 4,4′-ODA showed improved retention rates. CAF-M2P8 preserved 42 % of TS and 98 % of E after 24 h exposure to nitric acid compared to that of CAF-M10P0 (15 % and 61 %, respectively). In addition, under strongly alkaline conditions, CAF-M2P8 exhibited 90 % TS retention, 99 % *E* retention, and nearly 100 % retention of both properties in a steam environment. These results can be attributed to the compact packing of 4,4′-ODA-based polymer chains, as evidenced by a reduced d-spacing of crystal planes (Fig. 6d). The reduced d-spacing inhibits the penetration and subsequent diffusion of chemical species, thereby preventing surface etching and internal structural degradation [50]. This suggests that chain packing characteristics are the key factor determining environmental resistance rather than crystallinity or chain alignment.

Fig. 6e demonstrates the tunability of fiber properties by adjusting the monomer ratio, which covers the transition from extended chains to rigid and densely packed chains. Based on the above findings and the quantitative requisites summarized in Table S10, a rational performance grading was established to classify the CAFs according to their dominant property domains, ranging from high-strength/modulus to high thermo-chemical durability. The grading criteria were defined considering tensile performance and durability characteristics [51,52], providing a basis for evaluating composition-dependent transitions in fiber properties. Specifically, fibers with tensile strength $\geq$2.0 GPa and tensile modulus $\geq$50.0 GPa were classified as high-strength/modulus grade, while thermo-chemical durability was graded according to the retention rate of tensile strength under extreme environments, from None (90–100 %) to Degraded (0–19 %). This classification framework was further substantiated by comparison with representative commercial aramid fibers (Table S11). Kevlar® KM2+ demonstrated the most outstanding overall mechanical properties among conventional *p*-aramid fibers. Within the CAF series, CAF-M10P0, which shares the same composition as Technora®, exhibited nearly identical mechanical properties compared to the commercial fiber (tensile strength 3.1 GPa, modulus 80.4 GPa), thereby validating the reliability of our system. Conversely, the introduction of 4,4′-ODA resulted in lower tensile properties but markedly enhanced thermal and chemical resistance, surpassing all commercial aramid fibers. After heat treatment at 300 °C for 6 h, the CAF-M6P4 to CAF-M2P8 fibers retained approximately 90–100 % of their tensile strength, compared with ~70 % for Technora®. Furthermore, CAF-M2P8 exhibited approximately 2.8- and 1.6-fold higher retention of tensile strength and modulus, respectively, under harsh nitric acid exposure. These results demonstrate that CAFs can be systematically categorized into distinct high-strength/modulus and thermo-chemical grades through precise control of the ODA positional isomer ratio, establishing the core innovation of this work: a molecular design strategy enabling property tailoring of high-performance aramid fibers solely by regulating the ratio of positional isomers.

4. Conclusion

Fibers enriched with 3,4′-ODA exhibited outstanding mechanical performance for achieving a tensile modulus and tensile strength of 80.4 and 3.1 GPa, respectively, which can be attributed to enhanced chain alignment during the drawing process. This improvement is driven by increased linearity and flexibility imparted by the double-kinked structure of 3,4′-ODA. In contrast, fibers with a higher 4,4′-ODA content demonstrated superior thermal and chemical resistance, with a 25.7 °C increase in degradation temperature and a 42 % retention of tensile strength under acidic conditions; these advantages are attributed to rigid chain conformations and compact molecular packing.

These findings highlight the crucial role of the molecular configuration in determining the fiber microstructure and its resultant properties. This work establishes a scalable strategy to determine mechanical performance and thermo-chemical durability by tuning the monomer ratio during polymerization. Unlike conventional post-treatment techniques and broad-performance classification systems, the copolymerization approach enables fine-tuned application-specific performance grading. The resulting fibers are not only robust and reliable but also adaptable to demanding applications in aerospace, electric vehicles, and high-frequency optical systems, thereby offering a blueprint for the next generation of high-performance aramid fibers.

CRediT authorship contribution statement

Min Woo Kim: Writing – original draft, Investigation, Conceptualization. **Hyeonjeong Kim:** Visualization, Investigation, Data curation. **Jaegeun Lyu:** Investigation, Data curation. **Howon Choi:** Data curation. **Juyoung Kim:** Data curation. **Donghoon Lee:** Data curation. **Dae Young Lim:** Supervision. **Ji Ho Youk:** Writing – review & editing, Supervision. **Youngho Eom:** Writing – review & editing, Supervision. **Han Gi Chae:** Writing – review & editing, Supervision, Resources.

Declaration of competing interest

The authors declare the following financial interests/personal relationships which may be considered as potential competing interests: Youngho Eom reports financial support was provided by National Research Foundation. Youngho Eom reports financial support was provided by National Research Foundation. If there are other authors, they declare that they have no known competing financial interests or personal relationships that could have appeared to influence the work reported in this paper.

Acknowledgement

This work was supported by the National Research Foundation of Korea (NRF)(2021M3H4A3A01043764) and the Nano & Material

Technology Development Program through the NRF, funded by Ministry of Science and ICT (RS-2025-25442298).

Appendix A. Supplementary data

Supplementary data to this article can be found online at https://doi.org/10.1016/j.polymertesting.2025.109040.

Data availability

Data will be made available on request.

References

[1] A.K. Hamzat, M.S. Murad, I.A. Adediran, E. Asmatulu, R. Asmatulu, Fiber-reinforced composites for aerospace, energy, and marine applications: an insight into failure mechanisms under chemical, thermal, oxidative, and mechanical load conditions, Adv. Compos. Hybrid Mater. 8 (2025) 152, https://doi.org/10.1007/s42114-024-01192-y.

[2] S. Siengchin, A review on lightweight materials for defence applications: present and future developments, Def. Technol. 24 (2023) 1–17, https://doi.org/10.1016/j.dt.2023.02.025.

[3] A. Wazeer, A. Das, C. Abeykoon, A. Sinha, A. Karmakar, Composites for electric vehicles and automotive sector: a review, Green. Energy. Intell. Transp. 2 (2023) 100043, https://doi.org/10.1016/j.geits.2022.100043.

[4] B. Parveez, M.I. Kittur, I.A. Badruddin, S. Kamangar, M. Hussien, M.A. Umarfarooq, Scientific advancements in composite materials for aircraft applications: a review, Polymers 14 (2022) 5007, https://doi.org/10.3390/polym14225007.

[5] Z. Liu, Y. Wang, J. Yu, Y. Chen, M. Zhu, The past, present and future of high-performance fibers, Natl. Sci. Rev. 11 (2024) nwae310, https://doi.org/10.1093/nsr/nwae310.

[6] S. Simões, High-performance advanced composites in multifunctional material design: state of the art, challenges, and future directions, Materials 17 (2024) 5997, https://doi.org/10.3390/ma17235997.

[7] A. He, T. Xing, Z. Liang, Y. Luo, Y. Zhang, M. Wang, et al., Advanced aramid fibrous materials: fundamentals, advances, and beyond, Adv. Fiber Mater. 6 (2024) 3–35, https://doi.org/10.1007/s42765-023-00332-1.

[8] K. Li, X. Ni, Q. Wu, C. Yuan, C. Li, D. Li, H. Chen, Y. Lv, A. Ju, Carbon based fibers: fabrication, characterization and application, Adv. Fiber Mater. 4 (2022) 631–682, https://doi.org/10.1007/s42765-022-00134-x.

[9] H. Chang, J. Luo, P.V. Gulgunje, S. Kumar, Structural and functional fibers, Annu. Rev. Mater. Res. 47 (2017) 331–359, https://doi.org/10.1146/annurev-matsci-120116-114326.

[10] C. Chen, J. Feng, J. Li, Y. Guo, X. Shi, H. Peng, Functional fiber materials to smart fiber devices, Chem. Rev. 123 (2023) 613–662, https://doi.org/10.1021/acs.chemrev.2c00192.

[11] Y. Peng, Y. Cui, Thermal management with innovative fibers and textiles: manipulating heat transport, storage and conversion, Natl. Sci. Rev. 11 (2024) nwae295, https://doi.org/10.1093/nsr/nwae295.

[12] B. Chaudhary, T. Winnard, B. Oladipo, S. Das, H. Matos, Review of fiber reinforced composite structures with multifunctional capabilities through smart textiles, Textiles 4 (2024) 391–416, https://doi.org/10.3390/textiles4030023.

[13] H.H. Yang, Kevlar Aramid Fiber, John Wiley & Sons, Chichester, 1993.

[14] D. Tanner, J.A. Fitzgerald, B.R. Phillips, The Kevlar story – an advanced materials case study, Angew. Chem. Int. Ed. 28 (1989) 649–654, https://doi.org/10.1002/anie.198906491.

[15] H.G. Chae, S. Kumar, Rigid-rod polymeric fibers, J. Appl. Polym. Sci. 100 (2006) 791–802, https://doi.org/10.1002/app.22680.

[16] M. Jassal, S. Ghosh, Aramid fibres: an overview, Indian J. Fibre Text. Res. 27 (2002) 290–306.

[17] J.M. García, F.C. García, F. Serna, J.L. de la Peña, High-performance aromatic polyamides, Prog. Polym. Sci. 35 (2010) 623–686, https://doi.org/10.1016/j.progpolymsci.2009.09.002.

[18] M. Afshari, D.J. Sikkema, K. Lee, M. Bogle, High performance fibers based on rigid and flexible polymers, Polym. Rev. 48 (2008) 230–274, https://doi.org/10.1080/15583720802020129.

[19] S. Hayashida, Technora® fiber: super fiber from the isotropic solution of rigid-rod polymer, in: High Performance and Specialty Fibers: Concepts, Technology and Modern Applications of Man Made Fibers for the Future, Springer, Japan, Tokyo, 2016, pp. 149–169, https://doi.org/10.1007/978-4-431-55203-1_9, in: The Society of Fiber Science and Technology, Japan (Ed.).

[20] T. Jiang, J. Rigney, M.-C.G. Jones, L.J. Markoski, G.E. Spilman, D.F. Mielewski, D. C. Martin, Processing and characterization of thermally cross-linkable Poly[p-phenyleneterephthalamide-co-p-1,2-dihydrocyclobutaphenyleneterephthalamide] (PPTA-co-XTA) copolymer fibers, Macromolecules 28 (1995) 3301–3312, https://doi.org/10.1021/ma00113a035.

[21] X. Chen, Q. Sun, Y. Huang, W. Cai, Synthesis and properties of homopolyamide and copolyamides fibers based on 2,6-bis(p-aminophenyl)benzo[1,2-d;5,4-d′] bisoxazole, J. Appl. Polym. Sci. 110 (2008) 1891–1898, https://doi.org/10.1002/app.28811.

[22] L. Luo, Y. Wang, Y. Dai, Y. Yuan, C. Meng, Z. Cheng, X. Wang, X. Liu, The introduction of asymmetric heterocyclic units into poly(p-phenylene terephthalamide) and its effect on microstructure, interactions and properties, J. Mater. Sci. 53 (2018) 13291–13303, https://doi.org/10.1007/s10853-018-2580-1.

[23] L. Luo, Y. Yuan, Y. Dai, Z. Cheng, X. Wang, X. Liu, The novel high performance aramid fibers containing benzimidazole moieties and chloride substitutions, Mater. Des. 158 (2018) 127–135, https://doi.org/10.1016/j.matdes.2018.08.025.

[24] C. Yang, H. Wu, Y. Dai, D. Zhang, R. Xu, L. Luo, et al., Constructing mainstay body structure in heterocyclic aramid fiber to simultaneously improve tensile strength and toughness, Compos. B Eng. 202 (2020) 108411, https://doi.org/10.1016/j.compositesb.2020.108411.

[25] R. Xu, Y. Qiu, S. Tang, C. Yang, Y. Dai, D. Zhang, et al., Preparation of high strength and toughness aramid fiber by introducing flexible asymmetric monomer to construct misplaced Nunchaku structure, Macromol. Mater. Eng. 306 (2021) 2000814, https://doi.org/10.1002/mame.202000814.

[26] F. Xing, M. Zhang, Z. Wang, G. Sun, H. Niu, D. Wu, The introduction of benzimidazole and ether moieties into poly(p-phenylene terephthalamide): effects on its microstructure, interactions and properties, RSC Adv. 9 (2019) 33664–33673, https://doi.org/10.1039/C9RA07335C.

[27] H.G. Chae, D.Y. Lim, J.H. Youk, N.H. Park, D.J. Lim, H. Choi, et al.. KR102665659 (KITECH and UNIST), 2024.

[28] H. Jeong, J. Lyu, H. Choi, M.W. Kim, J. Kim, H. Yoo, et al., Enhanced thermal conductivity and mechanical property via improvement of hydrogen bonding between hexagonal boron nitride and aramid copolymer, Compos. Sci. Technol. 253 (2024) 110652, https://doi.org/10.1016/j.compscitech.2024.110652.

[29] S.M. Shebanov, I.K. Novikov, A.V. Pavlikov, O.B. Anańin, I.A. Gerasimov, IR and Raman spectra of modern aramid fibers, Fibre Chem. 48 (2016) 158–164, https://doi.org/10.1007/s10692-016-9761-y.

[30] L. Zhu, Y. Li, S. Han, H. Niu, D. Wu, S. Qi, Revealing the high-modulus mechanism of polyimide films prepared with 3,4′ ODA, Polymers 13 (2021) 3175, https://doi.org/10.3390/polym13183175.

[31] Y. Eom, B.C. Kim, The effect of dimethylsulfoxide on the dissociation process of physical complexes of polyacrylonitrile in N,N-dimethylformamide, Polym. Int. 66 (2017) 1099–1106, https://doi.org/10.1002/pi.5367.

[32] J. Lyu, H. Kim, M.W. Kim, J. Kim, H. Choi, D. Lee, D. Lim, J.H. Youk, Y. Eom, H. G. Chae, Optimizing p-aramid copolymer superfibers: the synergistic effect of solution rheology and fiber structure, Polym. Test. 152 (2025) 108987, https://doi.org/10.1016/j.polymertesting.2025.108987.

[33] M.A.Q. Al-Sayaghi, J. Lewis, C. Buelke, A.S. Alshami, Physicochemical and thermal effects of pendant groups, spatial linkages and bridging groups on the formation and processing of polyimides, Int. J. Polym. Anal. Char. 23 (2018) 566–576, https://doi.org/10.1080/1023666X.2018.1505221.

[34] S. Ran, D. Fang, X. Zong, B.S. Hsiao, B. Chu, P.M. Cunniff, Structural changes during deformation of Kevlar fibers via on-line synchrotron SAXS/WAXD techniques, Polymer 42 (2001) 1601–1612, https://doi.org/10.1016/S0032-3861(00)00460-2.

[35] S. Ran, X. Zong, D. Fang, B.S. Hsiao, B. Chu, P.M. Cunniff, R.A. Phillips, Studies of the mesophase development in polymeric fibers during deformation by synchrotron SAXS/WAXD, J. Mater. Sci. 36 (2001) 3071–3077, https://doi.org/10.1023/A:1017953412385.

[36] J. Blackwell, R.A. Cageao, A. Biswas, X ray analysis of the structure of HM 50 copolyamide fibers, Macromolecules 20 (1987) 667–671, https://doi.org/10.1021/ma00169a033.

[37] K. Tanaka, H. Kita, M. Okano, K.-i. Okamoto, Permeability and permselectivity of gases in fluorinated and non-fluorinated polyimides, Polymer 33 (1992) 585–592, https://doi.org/10.1016/0032-3861(92)90736-G.

[38] J. Puiggalí, Aliphatic polyamides (nylons): interplay between hydrogen bonds and crystalline structures, polymorphic transitions and crystallization, Polym. Cryst. 4 (2021) e10199, https://doi.org/10.1002/pcr2.10199.

[39] R. Tu, H.C. Kim, H.A. Sodano, Precipitation 3D printing of all-aramid materials for high-strength, heat-resistant applications, Mater. Des. 249 (2025) 113547, https://doi.org/10.1016/j.matdes.2024.113547.

[40] Q. Wang, Y. Bai, Y. Chen, J. Ju, F. Zheng, T. Wang, High performance shape memory polyimides based on π–π interactions, J. Mater. Chem. A 3 (2015) 352–359, https://doi.org/10.1039/C4TA05058D.

[41] Y.H. So, Rigid rod polymers with enhanced lateral interactions, Prog. Polym. Sci. 25 (2000) 137–157, https://doi.org/10.1016/S0079-6700(99)00038-6.

[42] A.F. Thünemann, W. Ruland, Microvoids in Polyacrylonitrile fibers: a small angle X ray scattering study, Macromolecules 33 (2000) 1848–1852, https://doi.org/10.1021/ma991427x.

[43] G. Song, S. Wang, D. Wang, H. Zhou, C. Chen, X. Zhao, et al., Rigidity enhancement of polyimides containing benzimidazole moieties, J. Appl. Polym. Sci. 130 (2013) 1653–1658, https://doi.org/10.1002/app.39324.

[44] X. Yu, W. Liang, J. Cao, D. Wu, Mixed rigid and flexible component design for high-performance polyimide films, Polymers 9 (2017) 451, https://doi.org/10.3390/polym9090451.

[45] H.G. Chae, S. Kumar, Making strong fibers, Materials science, Science 319 (2008) 908–909, https://doi.org/10.1126/science.1153911.

[46] M.G. Northolt, P. den Decker, S.J. Picken, J.J.M. Baltussen, R. Schlatmann, The tensile strength of polymer fibres, in: Advances in Polymer Science, 178, Springer, Berlin, 2005, pp. 1–108.

[47] T. Kitagawa, K. Yabuki, A.C. Wright, R.J. Young, An investigation into the relationship between processing, structure and properties for high-modulus PBO fibres: part 3: analysis of fibre microstructure using transmission electron microscopy, J. Mater. Sci. 49 (2014) 6467–6474, https://doi.org/10.1007/s10853-014-8377-y.

[48] J.R. Brown, B.C. Ennis, Thermal analysis of nomex® and kevlar® fibers, Textil. Res. J. 47 (1977) 62–66, https://doi.org/10.1177/004051757704700113.
[49] C. O'Connor, Acidic and basic amide hydrolysis, Chem. Soc. Rev. 24 (1970) 553–571, https://doi.org/10.1039/QR9702400553.
[50] S. Charati, A. Houde, S.S. Kulkarni, M. Kulkarni, Transport of gases in aromatic polyesters: correlation with WAXD studies, J. Polym. Sci. B Polym. Phys. 29 (1991) 921–931, https://doi.org/10.1002/polb.1991.090290803.
[51] Y. Hua, Y.-C. Yang, A. Yamanaka, Q.-Q. Ni, Low friction coefficient property of super fiber-reinforced composites, Adv. Compos. Mater. 20 (2011) 133, https://doi.org/10.1016/j.polymertesting.2025.108987.
[52] DuPont, *Kevlar*® Aramid Fiber Technical Guide, DuPont, 2019. https://www.dupont.com/news/kevlar-properties.html. (Accessed 17 October 2025).